JGR Atmospheres

RESEARCH ARTICLE
10.1029/2023JD038639

Key Points:

- A new algorithm, which performs well in identifying the spectral gap over the Arctic sea-ice surface, is proposed
- The characteristics of intermittency under different meteorological conditions are revealed
- The effects of intermittency on eddy-covariance fluxes are assessed

Correspondence to:
B. Han,
hanbo5@mail.sysu.edu.cn

Citation:
Liu, C., Yang, Q., Shupe, M. D., Ren, Y., Peng, S., Han, B., & Chen, D. (2023). Atmospheric turbulent intermittency over the Arctic sea-ice surface during the MOSAiC expedition. *Journal of Geophysical Research: Atmospheres*, *128*, e2023JD038639. https://doi.org/10.1029/2023JD038639

Received 4 FEB 2023
Accepted 12 JUL 2023

Author Contributions:
Conceptualization: Qinghua Yang
Data curation: Changwei Liu, Matthew D. Shupe
Formal analysis: Changwei Liu, Qinghua Yang, Matthew D. Shupe, Shijie Peng, Bo Han, Dake Chen
Funding acquisition: Qinghua Yang
Investigation: Changwei Liu
Methodology: Changwei Liu, Yan Ren
Project Administration: Qinghua Yang
Resources: Matthew D. Shupe
Supervision: Qinghua Yang, Dake Chen
Validation: Changwei Liu, Matthew D. Shupe, Yan Ren, Bo Han, Dake Chen
Visualization: Changwei Liu, Shijie Peng
Writing – original draft: Changwei Liu
Writing – review & editing: Changwei Liu, Qinghua Yang, Matthew D. Shupe, Yan Ren, Shijie Peng, Bo Han, Dake Chen

Atmospheric Turbulent Intermittency Over the Arctic Sea-Ice Surface During the MOSAiC Expedition

Changwei Liu[1], Qinghua Yang[1], Matthew D. Shupe[2,3], Yan Ren[4], Shijie Peng[1], Bo Han[1], and Dake Chen[1]

[1]School of Atmospheric Sciences, Sun Yat-sen University, and Southern Marine Science and Engineering Guangdong Laboratory (Zhuhai), Zhuhai, China, [2]Cooperative Institute for Research in Environmental Science, University of Colorado Boulder, Boulder, CO, USA, [3]NOAA Physical Science Laboratory, Boulder, CO, USA, [4]Collaborative Innovation Center for West Ecological Safety, Lanzhou University, Lanzhou, China

Abstract Turbulent motions in the Arctic stable boundary layer are characterized by intermittency, but they are rarely investigated due to limited observations, in particular over the sea-ice surface. In the present study, we explore the characteristics of turbulent intermittency over the Arctic sea-ice surface using data collected during the Multidisciplinary drifting Observation for the Study of Arctic Climate expedition from October 2019 to September 2020. We first develop a new algorithm, which performs well in identifying the spectral gap over the Arctic sea-ice surface. Then the characteristics of intermittency are investigated. It is found that the strength of intermittency increases under the conditions of light surface wind speed, small surface wind speed gradient, and strong surface air temperature gradient. The momentum flux, sensible heat flux, and latent heat flux calculated by raw eddy-covariance fluctuations are overestimated by 3%, 10%, and 24%, respectively, because submesoscale motions are included. Furthermore, the characteristics of the atmospheric boundary layer structure under various intermittency conditions reveal that strong low-level jets are favorable to surface turbulent motions that result in weak intermittency, while strong temperature inversions above the surface layer suppress surface turbulent motions and lead to strong intermittency.

Plain Language Summary In polar regions, turbulent mixing in the near-surface layer is weak and is often modulated by strong stable stratification, thus the intermittent state of turbulence is universal. The intermittency might lead to inaccuracy of the Monin-Obukhov similarity theory, which assumes that turbulence is fully developed. In this study, by using a year of eddy-covariance observations collected over the Arctic sea-ice surface, we first develop an automatic algorithm to identify the spectral gap where the Hilbert spectrum presents an abrupt drop in low frequency. Using only high-frequency turbulent motions, the turbulent data is reconstructed. This algorithm has the potential to quantify the characteristics of turbulence intermittency in polar regions. Based on our analysis, the intermittency results in the greatest relative influence on the latent heat flux compared with the momentum and sensible heat fluxes. Furthermore, we found the following meteorological conditions often lead to the enhancement of intermittency: low surface wind speed and wind speed gradient; strong surface air temperature gradient; weak low-level jets; and strong temperature inversions above the surface layer. These findings help to improve our understanding of turbulent intermittency over the Arctic sea-ice surface.

1. Introduction

In recent years, within the context of global climate change, the Arctic sea ice has also been undergoing rapid changes, and the Arctic has entered the "new Arctic" period (Kwok & Cunningham, 2015; Landrum & Holland, 2020). As one of the key processes of sea ice-atmosphere interactions, turbulent exchange plays an important role in the evolution of the Arctic sea ice (Andreas et al., 2010). The turbulent sensible and latent heat fluxes are essential components of the energy exchange over the sea-ice surface, impacting the sea ice thermodynamic state, while turbulent momentum flux directly affects the wind speed near the surface (Best et al., 2011) and the movement of sea ice. Hence, to understand the state of the Arctic sea ice and lower atmosphere, it is essential to accurately quantify turbulent exchanges. The eddy-covariance (EC) technique is considered the most direct and prevailing method to measure near-surface atmospheric turbulence (Aubinet et al., 2012; Peltola et al., 2021). In the Arctic region, however, the atmospheric surface layer is most often stably stratified, and the turbulence is weak and typically characterized by intermittency (Grachev et al., 2005; Lu et al., 2013; Salmond &

McKendry, 2005). As a result, the signal derived using the traditional EC method is almost always contaminated by nonstationary motions and becomes inappropriate for accurately describing the turbulent exchanges (Cava et al., 2019; Ren, Zhang, Wei, Wu, Cai, et al., 2019). Hence, this feature of near-surface motions, for example, intermittency, and how it affects the derivation of surface fluxes needs to be explored in the Arctic stable boundary layer.

The definition of turbulence intermittency varies substantially among studies (Acevedo et al., 2006; Coulter & Doran, 2002; Mahrt, 2009, 2014; Muschinski et al., 2004). Here, the term intermittency is referred to as "global intermittency" in Mahrt (1999). It is defined as the case where eddies are missing or suppressed at a scale that is larger than the large turbulent eddies but smaller than mesoscale motions. For this definition, intermittency is induced by nonstationarities, such as internal gravity waves (Sun et al., 2015), horizontal meandering (Mortarini et al., 2019), and microfronts (Mahrt, 2019). These motions have a larger timescale than turbulence and sometimes are collectively referred to as submesoscale motions. Many previous studies have reported the existence of a spectral gap between the submesoscale and turbulent parts of the spectrum (Fiedler & Panofsky, 1970; Mahrt, 2007; Mahrt & Bou-Zeid, 2020; Wei & Zhang, 2013). Hence, the characteristics of turbulent intermittency can be investigated via spectral analysis of EC data. Vickers and Mahrt (2006) developed a multiresolution decomposition method to separate the turbulent and submesoscale motions based on multiresolution cospectra, and suggested a variable time window to calculate turbulent fluxes using the EC method. Acevedo et al. (2014) also used the same method to identify the contributions of submesoscale motions to spectra from six different observation sites. They found that turbulent kinetic energy increased exponentially with the time scale in the submesoscale range, and the increased rate was larger under weak turbulence situations. Although multiresolution spectra satisfy Reynolds averaging at all scales and do not assume periodicity unlike Fourier spectra (Howell & Mahrt, 1997), the multiresolution basis set is a wavelet basis set with a constant basis function (Wei et al., 2021). Recently, the Hilbert-Huang transform, which satisfies adaptivity, is emerging as a useful tool to study turbulence in view of the advantages of processing the nonstationary and nonlinear turbulent signal (Helmis et al., 2015; Huang et al., 2011; Ren, Zhang, Wei, Wu, Cai, et al., 2019; Ren, Zhang, Wei, Wu, Liu, et al., 2019; Schmitt et al., 2009; Wei et al., 2017, 2018, 2020).

Previous studies on turbulence intermittency mainly focused on the nocturnal stable boundary layer (Cava et al., 2017; Mahrt & Bou-Zeid, 2020; Monahan et al., 2015), and sporadic studies concerned the polar stable boundary layer (van den Kroonenberg and Bange, 2007). Allouche et al. (2022) investigated the detection, genesis, and modeling of turbulence intermittency by using the data collected over the snowpack surface in Utqiagvik, Alaska. They developed approaches to detect intermittency based on time series of the turbulence kinetic energy, and improved a flux model by introducing the vertical velocity variance in combination with different mixing length scales under different turbulence regimes. In addition, Ansorge and Mellado (2014, 2016) employed direct numerical simulations to reveal the effects of intermittency on the applicability of conventional paradigms (such as Monin-Obukhov similarity theory). So far, few studies have reported the characteristics of turbulent intermittency under the "new Arctic" sea-ice conditions in the central Arctic. To support the urgent need for understanding and modeling the rapidly changing Arctic atmosphere-ice-ocean system, a year-long expedition named the Multidisciplinary drifting Observation for the Study of Arctic Climate (MOSAiC) was designed to collect a wealth of observational data. The MOSAiC expedition was conducted from October 2019 to September 2020 in the central Arctic. A comprehensive and complementary atmospheric observational program during the expedition provides a unique opportunity to study turbulent intermittency in the Arctic stable boundary layer. More details about the atmospheric observations can be found in Shupe et al. (2022).

In this study, we develop a spectral gap identification algorithm based on Hilbert spectra which we use to reveal the characteristics of turbulent intermittency over the Arctic sea-ice surface using data collected during the MOSAiC expedition. We organize the paper as follows: the observational data and methods are described in Section 2; in Section 3, we present the results and discussion about statistical characteristics of intermittent strength, effects of the intermittency on turbulent fluxes derived from the EC method, and impacts of the atmospheric boundary layer structure on the intermittency; finally, a summary is given in Section 4.

2. Materials

2.1. Observation Data

The conventional meteorological and turbulence data are collected from a meteorological tower of 10-m height installed over the sea-ice surface during the MOSAiC expedition (Cox et al., 2021, 2023). This tower was located

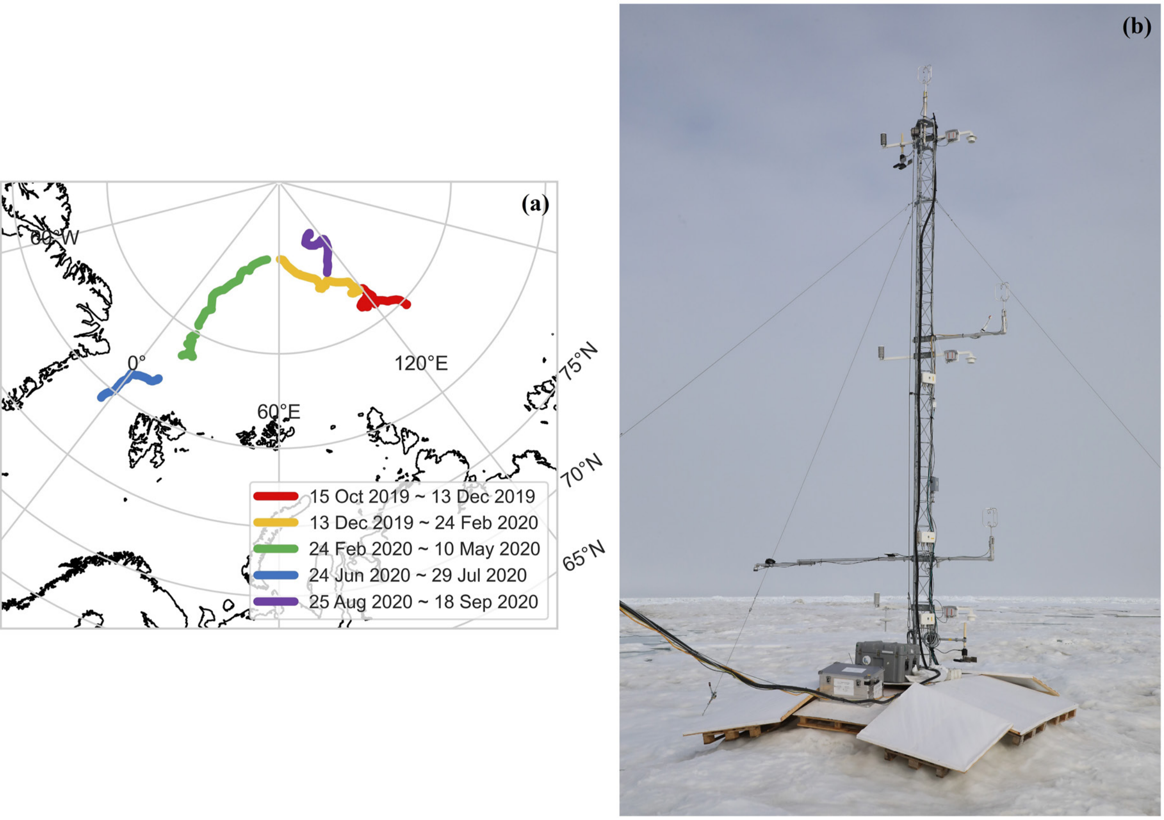

Figure 1. (a) The drift track and corresponding period of the meteorological tower during the MOSAiC expedition and (b) the instruments installed on the meteorological tower.

300–600 m from the research vessel Polarstern (Knust, 2017), which served as the base of operations for the expedition. Three levels of air temperature and humidity sensors (HMT330, Vaisala, Finland) and sonic anemometers (u-Sonic-3 Cage MP, METEK GmbH, Germany) were installed at the nominal heights of 2, 6, and 10 m on the 10-m meteorological tower, and an open-path optical gas analyzer (7500-DS, LI-COR, USA) was fixed at a nominal 2-m height for the winter-spring season, and a nominal 6-m height for October 2019 and June-September 2020. The three-dimensional wind and ultrasonic temperature data collected at the same level as the LI-COR 7500-DS location are jointly used to derive latent heat flux. The turbulent data observed at a nominal 2-m height are used to quantify intermittency. The sampling frequency of fast response instruments (i.e., u-Sonic-3 Cage MP anemometer and LI-COR 7500-DS) was at 20 Hz, resampled to 10 Hz. The presence of precipitation was measured by an OTT Parsivel2 laser disdrometer deployed by the US Department of Energy (DOE) Atmospheric Radiation Measurement (ARM) program (Wang et al., 2019). Additionally, a processed radiosounding data set was used from the Interpolated Sonde value-added product produced by ARM (Jensen et al., 2019), which was synthesized by multiple sources of sounding data (including radiosondes, ceilometer, and others) observed onboard Polarstern. Only the data collected during the period when the vessel passively drifted with an ice floe are used in this study, and the corresponding drift track of the meteorological tower and instruments are presented in Figure 1.

We conduct the data processing for raw turbulence, including error flag detection, despiking, true wind correction, coordinate rotation via double rotation, block averaging over a 30-min interval, and then the turbulent fluxes are derived over 30-min periods. To ensure the reliability of eddy-covariance data, we use the following data acceptance criteria: no precipitation occurs during the half-hour in question, the dip angle of the attitude indicator is smaller than 1°, winds come from angles [0–170°] and [190–360°] relative to the sonic coordinate system, and more than 80% of the 10 Hz data is present for each half-hour. The corresponding data from slow response measurements are averaged every half-hour. No gap-filling is performed in this study.

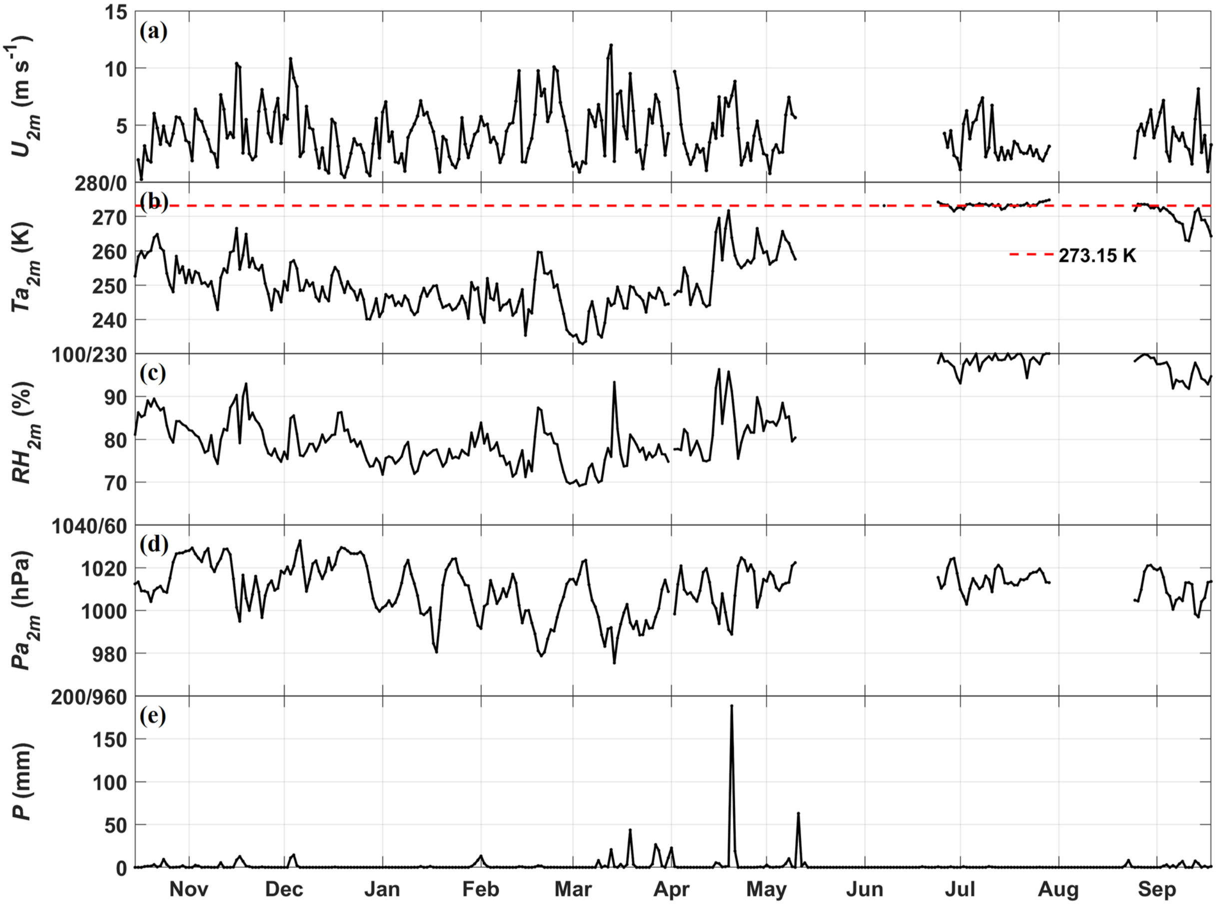

Figure 2. Meteorological data collected during the MOSAiC expedition. Panels (a–d) are the time series of daily wind speed, air temperature, relative humidity, and presence of precipitation, respectively.

2.2. Conventional Meteorological Conditions

Figure 2 shows the conventional meteorological conditions of daily mean 2-m wind speed (U_{2m}), 2-m air temperature (Ta_{2m}), 2-m relative humidity (RH_{2m}), and precipitation occurrence (P) during the MOSAiC expedition. There are about 71 days, which are concentrated in the period from 11 May 2020 to 23 June 2020 and from 30 July 2020 to 24 August 2020, that are missing due to the transit of Polarstern. From the available data collected during the passive drifting period, we conclude that: (a) the mean U_{2m} during the MOSAiC expedition was 4.2 m s^{-1}, and the monthly mean U_{2m} reached its maximum (minimum) of 5.4 m s^{-1} (3.3 m s^{-1}) in February (July); (b) in the coldest month March, the monthly mean Ta_{2m} was 242.9 K, while the daily mean Ta_{2m} began to approach 273.15 K in late June; (c) RH_{2m} showed a significant positive correlation with the variation of Ta_{2m}, so it is at its minimum in March and maximum in July (>98%) when the sea-ice surface melted; and (d) there were 105 days when precipitation occurred during the whole observation period, with most concentrated in autumn and spring.

2.3. Turbulent Parameters

The turbulent parameters used in this study include the turbulent fluxes, the stability parameter, and the local intermittent strength of turbulence. The turbulent fluxes are calculated using the eddy-covariance method (named EC fluxes hereafter):

$$\tau = \rho u_*^2 \tag{1}$$

$$\mathrm{SH} = c_p \rho \overline{w'\theta'} \tag{2}$$

$$\mathrm{LE} = \lambda \rho \overline{w'q'} \tag{3}$$

$$u_* = \left(\overline{u'w'}^2 + \overline{v'w'}^2\right)^{1/4} \tag{4}$$

where τ (N m^{-2}), SH (W m^{-2}), and LE (W m^{-2}) are the turbulent momentum flux, sensible heat flux, and latent heat flux, respectively, ρ (kg m^{-3}) is the air density, c_p (=1,004.7 J kg^{-1} K^{-1}) is the constant-pressure specific heat capacity of air, λ (=2.5×10^6 J kg^{-1}) is the latent heat of vapourization, u' (m s^{-1}), v' (m s^{-1}), w' (m s^{-1}), θ' (K), and q' (kg kg^{-1}) are the turbulent fluctuations of streamwise wind speed, crosswind speed, vertical wind speed, potential temperature, and specific humidity, respectively.

The stability parameter used to quantify the stability of atmospheric stratification in this study is the bulk Richardson number (Ri_b). It can be derived as follows:

$$Ri_b = g_v(z_2 - z_1)\frac{(Ta_{6m} - Ta_{2m}) \times 2}{(Ta_{6m} + Ta_{2m})(U_{6m} - U_{2m})^2} \tag{5}$$

where, Ta_{6m} (K) and U_{6m} (m s^{-1}) are the air temperature and wind speed collected at the observation height of z_2 (=6 m), and $g_v = 9.8$ m s^{-2} is the gravity.

The index to quantify the local intermittent strength of turbulence (LIST) in this study is consistent with that of Ren, Zhang, Wei, Wu, Cai, et al. (2019):

$$\mathrm{LIST} = \frac{v_{\text{turb}}}{\sqrt{V_{\text{turb}}{}^2 + \mathrm{V}_{\text{smeso}}{}^2}} \tag{6}$$

$$V_{\text{turb}} = \sqrt{u'_{\text{turb}}{}^2 + v'_{\text{turb}}{}^2 + w'_{\text{turb}}{}^2} \tag{7}$$

$$V_{\text{smeso}} = \sqrt{u'_{\text{smeso}}{}^2 + v'_{\text{smeso}}{}^2 + w'_{\text{smeso}}{}^2} \tag{8}$$

where, V_{turb} and V_{smeso} represent the strength of turbulent and submesoscale motions, respectively. These two motions can be separated once a spectral gap is identified between them. It can be seen from Equation 6 that larger LIST values approaching the maximum value of 1 indicate the dominance of turbulent components in the acquired signal, while smaller LIST values mean greater effects of submesoscale motions and stronger intermittency.

2.4. A New Algorithm to Identify the Spectral Gap

Compared with the fast Fourier transform and the wavelet transform for spectrum analysis, the Hilbert-Huang transform presents notable advantages in processing nonstationary and nonlinear turbulent signals (Wei et al., 2017). The location of the spectral gap should be characterized by the significant drop before the spectral gap and the relative flat slope after the spectral gap in the second-order Hilbert spectrum. Accordingly, Ren, Zhang, Wei, Wu, Cai, et al. (2019) developed an automated algorithm to identify the spectral gap under heavy haze pollution conditions based on the second-order Hilbert spectrum analysis by using the data collected over urban and suburban surfaces. However, when we use their algorithm to identify the spectral gap over the snow or sea-ice surfaces in the Arctic, we find it always fails to identify the spectral gaps that are located at $\log(\omega) > -2.5$ (here ω is the frequency). Because it takes the smallest $\log(\omega \cdot Hs)$ found in the range of $\log(\omega) < -2.5$ as the priority (here Hs is the second-order Hilbert spectral value), the algorithm misses the "true" spectral gap if it is located at $\log(\omega) > -2.5$. In this study, we update the algorithm to identify the spectral gap as follows: (a) Decomposing the fluctuation of measured elements (i.e., u', v', w', θ', q') during each 30-min period into intrinsic model functions (IMF) by using the empirical mode decomposition method (Rilling et al., 2003). (b) Calculating the second-order Hilbert spectrum of IMF (Huang et al., 2008). (c) As the submesoscale parts of the spectrum should not be located at too high frequencies, the location of the spectral gap is assumed to be at a frequency of $\log(\omega)$ lower than -1.5, the same as in Ren, Zhang, Wei, Wu, Cai, et al. (2019). Accordingly, to identify the potential location of the spectral gap, the frequency locations of local minima of $\omega \cdot Hs$ across the frequency range of $\log(\omega) < -1.5$ are labeled. (d) To quantify the abrupt drop of $\omega \cdot Hs$ before the frequencies identified in step (c), the difference between the present minimum $\omega \cdot Hs$ and previous maximum $\omega \cdot Hs$ (i.e., $\nabla \log(\omega \cdot Hs)$) is calculated. (e) To ensure the drop of $\omega \cdot Hs$ before the spectral gap is significant enough and the slope of $\log(Hs)$

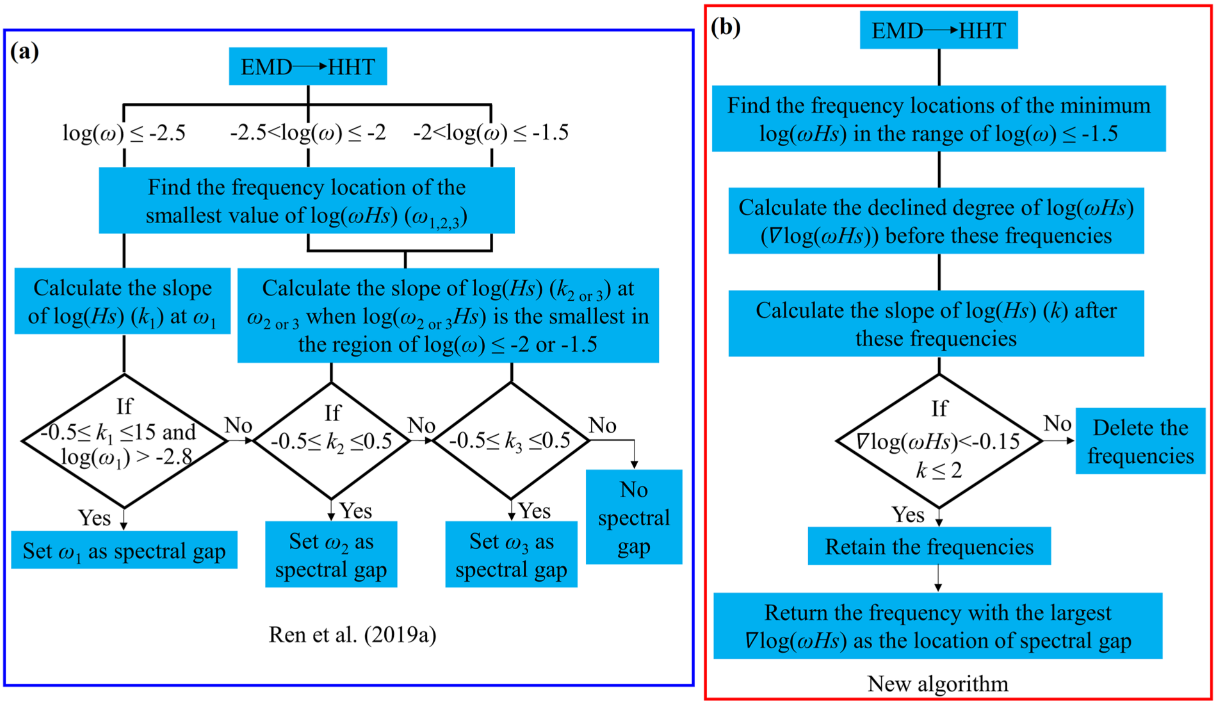

Figure 3. The flowcharts of Ren, Zhang, Wei, Wu, Cai, et al. (2019)'s algorithm (a) and the newly developed algorithm in this study (b).

(k) after the spectral gap is relative flat, the frequencies with $\nabla\log(\omega{\cdot}Hs) > 0.15$ and $k < 2$ are retained. (f) The frequency with the most significant drop of $\omega{\cdot}Hs$ (i.e., the largest $\nabla\log(\omega{\cdot}Hs)$) is selected as the location of the spectral gap. It should be noted that the thresholds of 0.15 for $\nabla\log(\omega{\cdot}Hs)$ and 2 for k are determined empirically. To derive the optimal values of the thresholds, the samples on the first and fifteenth of each month are picked out, and the locations of the spectral gap for these samples are identified by visual inspection. Then, we adjust values of the thresholds to make the results from the automatic algorithm agree well with the results from visual inspection. Figure 3 gives the flowcharts of Ren, Zhang, Wei, Wu, Cai, et al. (2019)'s algorithm and our updated algorithm. Comparing with their algorithm, we introduce the $\nabla\log(\omega{\cdot}Hs)$ to ensure the characteristics of shape decline before the spectral gap and revise the threshold of the slope of log (Hs).

Once the spectral gap is identified, we search for the IMF mode (N) with the mean frequency closest to the spectral gap. Then modes 1–N are chosen to reconstruct the signal of turbulent motions, and the other modes are used to reconstruct the submesoscale signal. As in the example shown in Figure 4, it can be found that in the inertial sub-range, the spectra of u', v', and w' follow the −5/3 power law well, which indicates the validity of the Hilbert-Huang transform for spectral analysis and the high quality of the observational data. For the spectrum of u', Ren, Zhang, Wei, Wu, Cai, et al. (2019)'s algorithm fails to identify the existence of a spectral gap, while our algorithm can capture the sharp decline of $\log(\omega{\cdot}Hs)$ ahead of the frequency of 0.0045 Hz where the spectral gap should exist. The spectrum of reconstructed turbulent motions of u' is more consistent with the classic spectral pattern for turbulence. For the spectra of v' and w', our algorithm identifies the location of the spectral gap at higher frequencies to obtain a purer reconstructed turbulent signal. In this case, our algorithm also produces reasonable frequency locations of the spectral gap for θ', and q' (not shown in Figure 4). In fact, the superiority of the new algorithm is not only reflected in this example, but also demonstrated by most samples. Hence, we conclude that the new algorithm performs better in identifying the spectral gap over the Arctic sea-ice surface.

3. Results and Discussion

3.1. Statistical Characteristics of LIST

During the whole observation period, we have 11,383 (11,383, 11,383, 11,505, 5,791) samples of 30-min streamwise wind speed (crosswind speed, vertical wind speed, potential temperature, specific humidity) data. The proportion of spectral gaps identified in u', v', w', θ', and q' is 76%, 82%, 57%, 81%, and 80%, respectively. Thus,

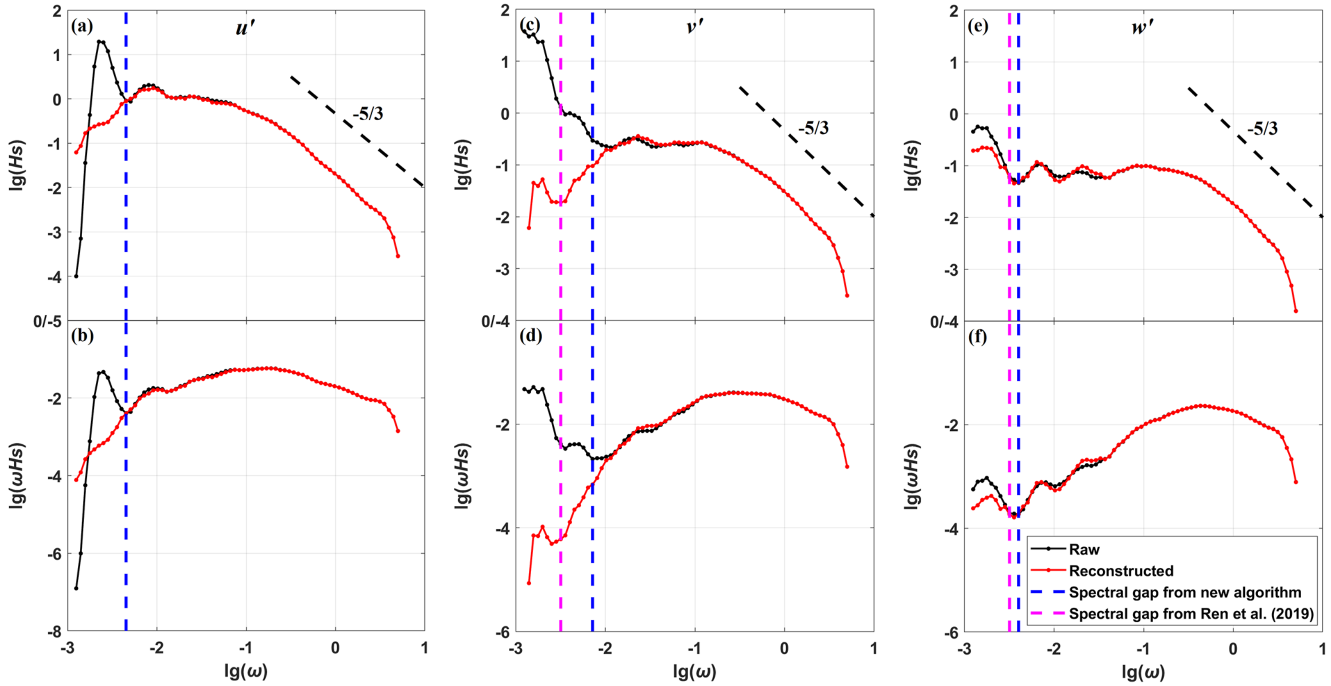

Figure 4. The second-order Hilbert spectra of three wind speed components u' (a, b), v' (c, d), and w' (e, f) at 09:30 on 10 November 2019. The upper panels show the spectra of Hs, while the lower panels show the spectra of ωHs. The magenta and blue dashed lines indicate the locations of the spectral gap identified by Ren, Zhang, Wei, Wu, Cai, et al. (2019) and our new algorithm, respectively. The solid black lines are the spectra from raw data, and the solid red lines represent the spectra from reconstructed data for pure turbulence according to the spectral gap identified by our new algorithm.

the occurrence of a spectral gap is common throughout the MOSAiC expedition, which means that the effects of nonstationary motions on the collected signal are significant. In addition, our results indicate a higher proportion of spectral gaps in u', v', w', θ', and q' than reported by Ren, Zhang, Wei, Wu, Cai, et al. (2019) for the heavy pollution conditions in Beijing. There are two potential reasons for this difference. One is that the new algorithm updates the criteria of spectral gap identification; the other is that the influence of submesoscale motions is stronger under the weak turbulence conditions in the Arctic. The high proportion of spectral gaps over the 30-min intervals indicates that the 30-min time length conventionally used in the calculation of eddy-correlation fluxes is not often suitable in these conditions. The mean frequency of the spectral gap for u', v', w', θ', and q' is located at 0.0047, 0.0046, 0.0034, 0.0051, and 0.0053 s^{-1}, respectively. Hence, a partial gap between turbulence scales and submeso scales occurs at a time scale of 3–5 min, which is consistent with Mahrt (2009). However, van den Kroonenberg and Bange (2007) presented gaps at much smaller time scales ranging from a few seconds to tens of seconds for the cospectra of the sensible heat flux and latent heat flux by using data collected over sea-ice in the Arctic summer.

On the other hand, we find that there are 352 samples wherein no spectral gap occurred in u', v', and w' (i.e., $V_{\mathrm{smeso}} = 0$ and LIST = 1). As shown in Figure 5 (a), the distribution of samples with LIST = 1 in each bin of U_{2m} (with an interval of 1 m s^{-1} for each bin) is presented. It can be seen that the number of samples ($n = 60$) in the range of 5 m s^{-1} to 6 m s^{-1} is the largest, while the proportion of cases where LIST = 1 increases with increasing wind speed, which means that the probability of pure turbulent motions persisting throughout the 30-min acquired signal is higher under strong wind conditions. In addition to U_{2m}, we also investigate the distribution of samples with LIST = 1 under different $U_{6m} - U_{2m}$, $Ta_{6m} - Ta_{2m}$, and Ri_b conditions. Our results show that the conditions with a large wind speed gradient, small air temperature gradient, and near-neutral stratification are most common for the occurrence of LIST = 1.

Furthermore, Figure 6 demonstrates the relationships between LIST and conventional meteorological conditions. It is clear that LIST increases with the increase of wind speed (Figure 6a), where an inverse trigonometric relationship of LIST = 0.23 × (1 + 2.3 × atan(0.8 × U_{2m})) is found. The mean LIST is 0.6 when $U_{2m} < 2$ m s^{-1}, while it reaches 0.9 when $U_{2m} \geq 2$ m s^{-1}. These results suggest that submesoscale motions produce a significant effect, and the intermittency is stronger under light wind speed conditions. Based on an analysis of the vertical turbulence spectrum, Li et al. (2020) also found that lower wind speed could suppress the large-scale eddies from

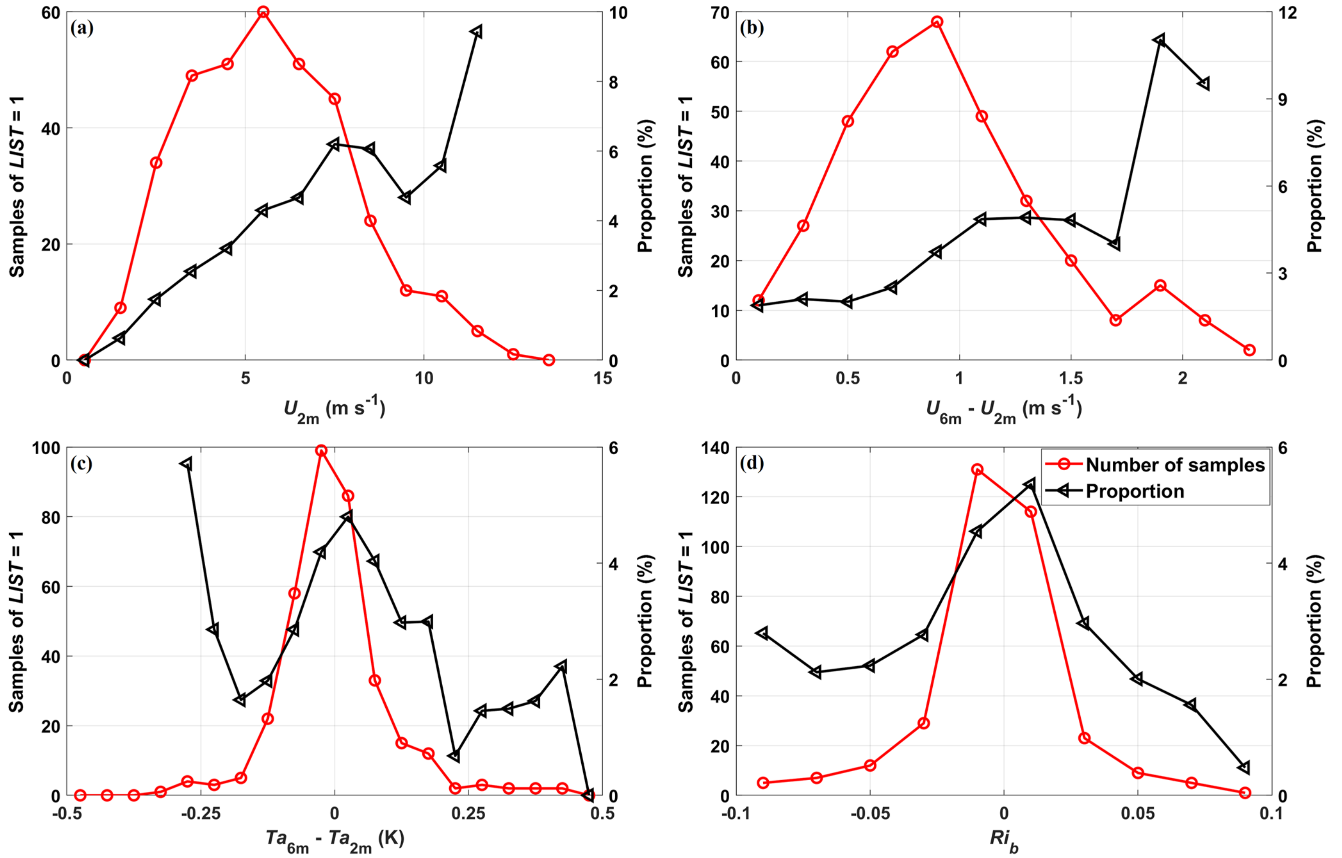

Figure 5. Samples of LIST = 1 under different (a) wind speed, (b) gradient of wind speed, (c) gradient of air temperature, and (d) stability conditions. The red line is the number of samples in each bin (scaled to the left y-axis), and the black line is the proportions of LIST = 1 in each bin (scaled to the right y-axis). Noted that only the proportions with total samples larger than 50 in a bin are shown in this figure. The bin intervals for $U_{6m} - U_{2m}$, $Ta_{6m} - Ta_{2m}$, and Ri_b are 0.2 m s^{-1}, 0.05 K, and 0.02, respectively.

breaking into small eddies, which resulted in an increased percentage of large-scale eddies under light wind speed conditions. There are no obvious relationships between LIST and Ta_{2m} or RH_{2m}, apart from decreased values for $Ta_{2m} \leq 233.6$ K and $RH_{2m} \leq 68.75\%$, where there are very few samples (Figures 6b and 6c). Figure 6d presents the variation of LIST with wind speed gradient $U_{6m} - U_{2m}$. It can be seen that the samples are concentrated in the range of 0 m s^{-1} $< U_{6m} - U_{2m} \leq 1.7$ m s^{-1} ($n = 10{,}467$), and LIST increases with the increase of wind speed gradient in this range. When $U_{6m} - U_{2m} > 1.7$ m s^{-1}, the LIST value tends to be a constant of 0.97, although with relatively few samples. The magnitude of the wind speed gradient reflects the intensity of momentum exchange between the surface and atmosphere. Hence, these results indicate that the intermittency is stronger under weaker momentum exchange conditions. Similar results can be found in Wei et al. (2018) and Allouche et al. (2022). We also investigate the variation of LIST with air temperature gradient $Ta_{6m} - Ta_{2m}$. As shown in Figure 6e, LIST reaches its maximum when $Ta_{6m} - Ta_{2m}$ is close to 0 K, while it reaches its lowest values in the range of $Ta_{6m} - Ta_{2m} > 1$ K ($n = 362$). Thus, the thermal condition of a large (small) air temperature gradient is favorable to submesoscale (turbulent) motions. Finally, the relationship of LIST to Ri_b is given in Figure 6f. The results show that the intermittency under stable stratification ($Ri_b > 0.1$) is stronger than that under unstable stratification ($Ri_b < -0.1$), and the turbulent signal under near-neutral stratification ($-0.1 \leq Ri_b \leq 0.1$) is the purest. Our results showing the dependence of intermittency on Richardson number are the same as reported by previous studies of near-surface measurements (e.g., Doran, 2004; Drüe & Heinemann, 2007; Mahrt, 2010).

3.2. Effects of Intermittency on EC Fluxes

To assess the effects of intermittency on EC fluxes, we compared the EC fluxes derived from raw data to those derived from reconstructed data. The fluxes derived from the reconstructed data (i.e., pure turbulent fluctuations)

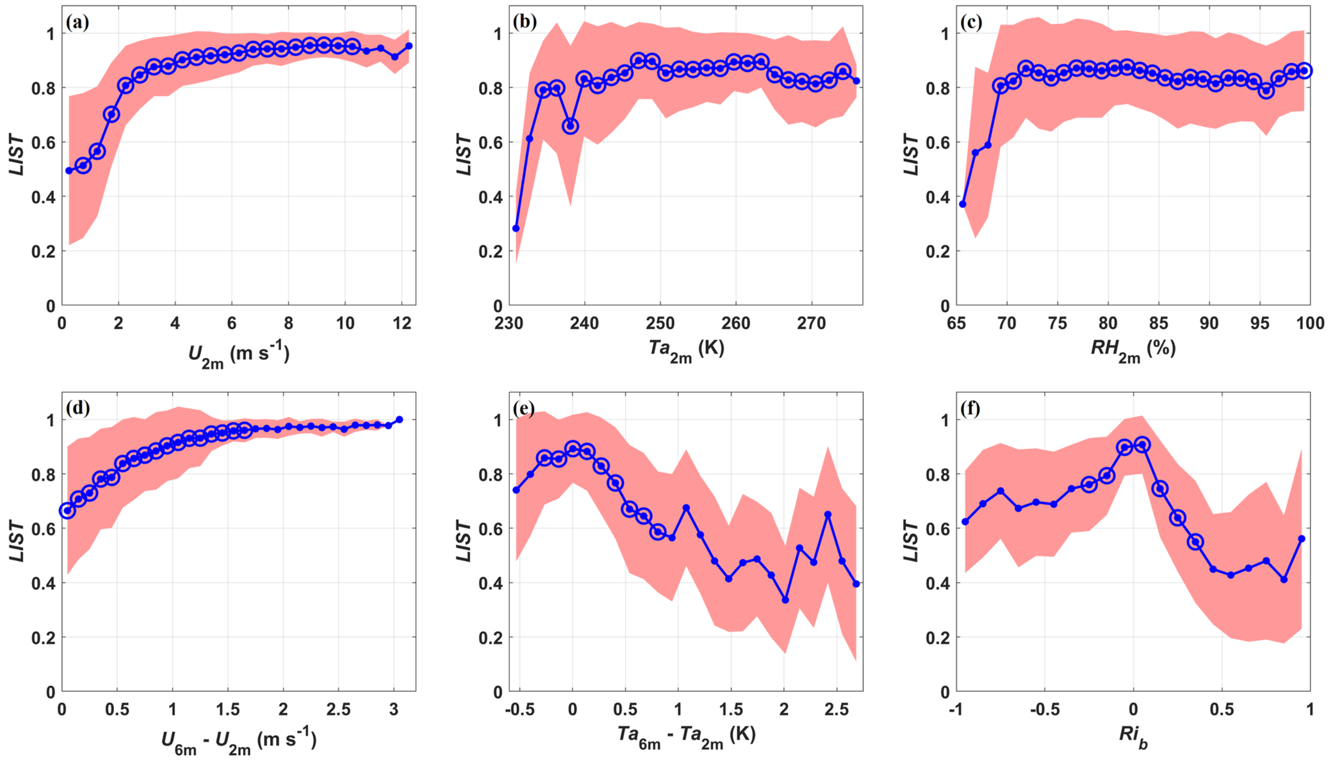

Figure 6. The variation of LIST with (a) U_{2m}, (b) Ta_{2m}, (c) RH_{2m}, (d) $U_{6m} - U_{2m}$, (e) $Ta_{6m} - Ta_{2m}$, and (f) Ri_b. The shaded areas represent the standard deviation, and the blue circles indicate that the number of samples in the bin is larger than 50.

are referred to as the reconstructed fluxes, and those from the raw data (submesoscale motions are included) are referred to as the original fluxes in Figure 7. Overall, the results indicate that the original fluxes are greater than the reconstructed ones. Compared with other fluxes, the smallest overestimation of 3% (i.e., the slope of the best-fit line in the comparison is 0.97) is found for the momentum flux (Figure 7a). The mean difference, defined as $|$original flux $-$ reconstructed flux$|/n$, for τ is 0.01 N m^{-2}. For the sensible heat flux (Figure 7b), the original flux is approximately 10% larger than the reconstructed flux (slope of 0.9) and the mean difference between the original SH and the reconstructed SH is 1.5 W m^{-2}. On the other hand, there are 506 samples located in the Beta and Delta quadrants (i.e., the original SH and the reconstructed SH show opposite sign) in Figure 7b, which means that the intermittency reverses the direction of SH in 4.7% of the samples. The slope of the best-fit line is 0.76 for the LE, as Figure 7c shows, which indicates that the LE calculated by the conventional method is overestimated by approximately 24%. The overestimation of LE is the most significant in terms of percentage difference. In addition, 6% of the LE samples are located in the Beta and Delta quadrants in Figure 7c.

Many previous studies supported the notion that submesoscale motions can strengthen the air-surface exchange of momentum, heat, and mass fluxes (Vickers & Mahrt, 2003, 2006; van den Kroonenberg and Bange, 2007; Mahrt, 2010; Wei et al., 2018; Ren, Zhang, Wei, Wu, Cai, et al., 2019). For example, in the polar regions, van den Kroonenberg and Bange (2007) presented an enhancement of 8% and 16% for the SH and LE by mesoscale motions, respectively, based on the analysis of multiresolution cospectra during the ARK-XII summer expedition (July-September 1996). Although a different method was used to identify the cospectral gap in their study, they similarly reported that quantitatively the effects of nonstationary motions on the LE were more significant than that on the SH. Ren, Zhang, Wei, Wu, Cai, et al. (2019) also found overestimation in original fluxes; however, they found overestimations of 13%, 12%, and 15% for τ, SH, and LE, respectively. Hence, compared with our results, Ren, Zhang, Wei, Wu, Cai, et al. (2019) presented a smaller overestimation for the latent heat flux but a larger overestimation for the momentum flux. Submesoscale motions vary significantly under different underlying surface and meteorological conditions (Mahrt, 2010). It is necessary to clarify the dynamics of submesoscale flow to explain the different effects of submesoscale motions under different conditions. However, the dynamics of submesoscale motions are still not clear. Sorbjan and Czerwinska (2013) considered gravity waves as the main

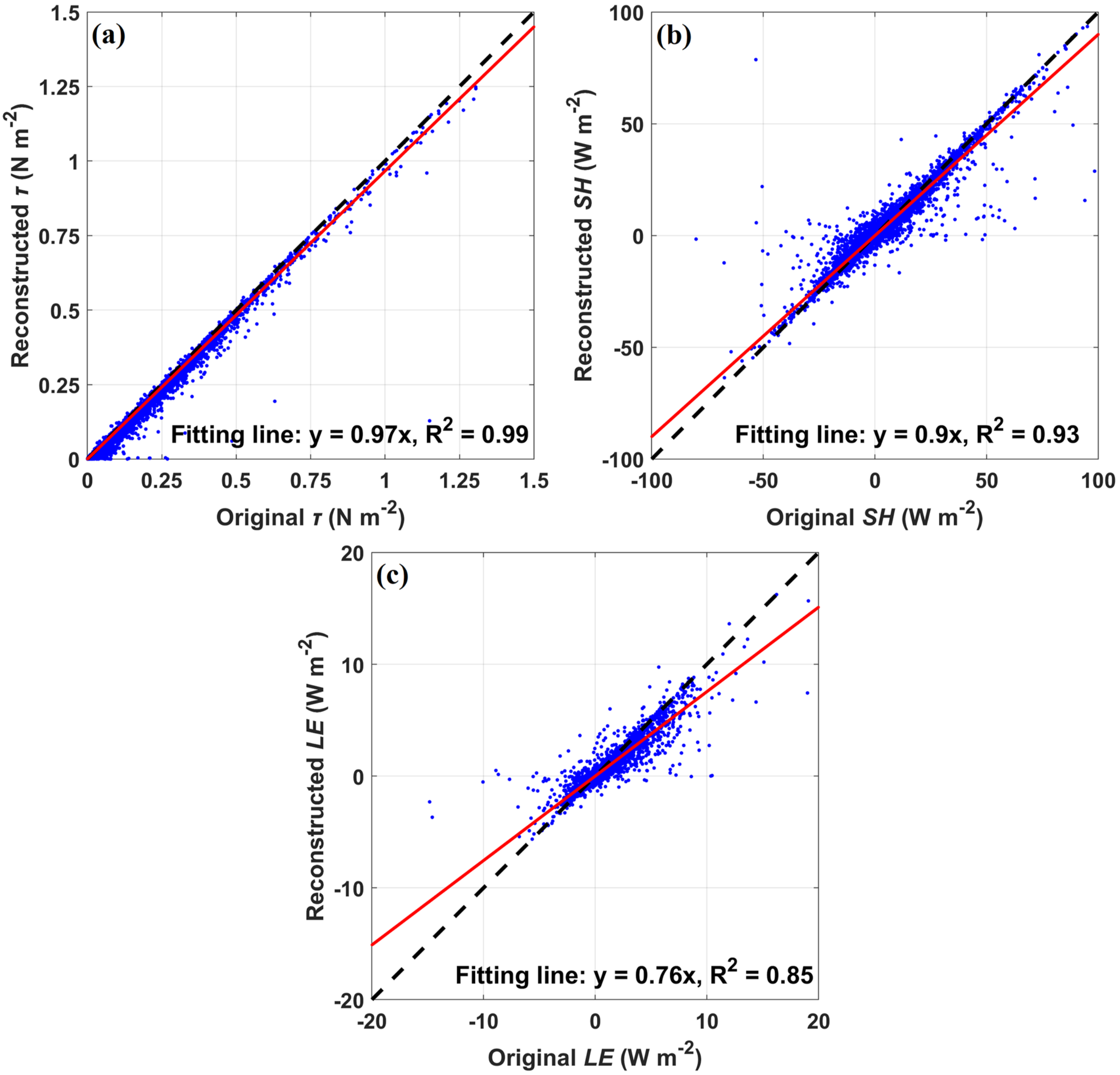

Figure 7. The comparison of turbulent fluxes derived from raw data and reconstructed data. The red lines are the best-fit lines.

source of submesoscale motions. While Wei et al. (2018) indicated that the wind shear produced by Low-Level Jets (LLJs) suppressed submesoscale motions in the near-surface layer. Other dynamics related to submesoscale motions such as free-flow stability (Zilitinkevich & Calanca, 2000), solitary waves (Terradellas et al., 2005), and low-frequency horizontal wind oscillations (Anfossi et al., 2005) have also been mentioned in previous studies.

3.3. Effects of the Atmospheric Boundary Layer Structure on Intermittency

3.3.1. The Role of Low-Level Jets (LLJs)

Figure 8a presents the vertical structure of horizontal wind speed within the boundary layer under different intermittency conditions. The Q1, Q2, …, and Q10 mean the samples of wind profiles located in the bins of the [0 10%], [10% 20%], …, and [90% 100%] quantiles of LIST. Thus, there is a decreasing intermittency from Q1 to Q10. From the perspective of the entire atmospheric boundary layer, the intermittency increases as the mean wind speed of the whole boundary layer decreases, ranging from 11.8 m s^{-1} in Q10 to 4.9 m s^{-1} in Q1. Van de Wiel et al. (2012) also indicated that continuous turbulence tended to be suppressed under light wind speed conditions in the

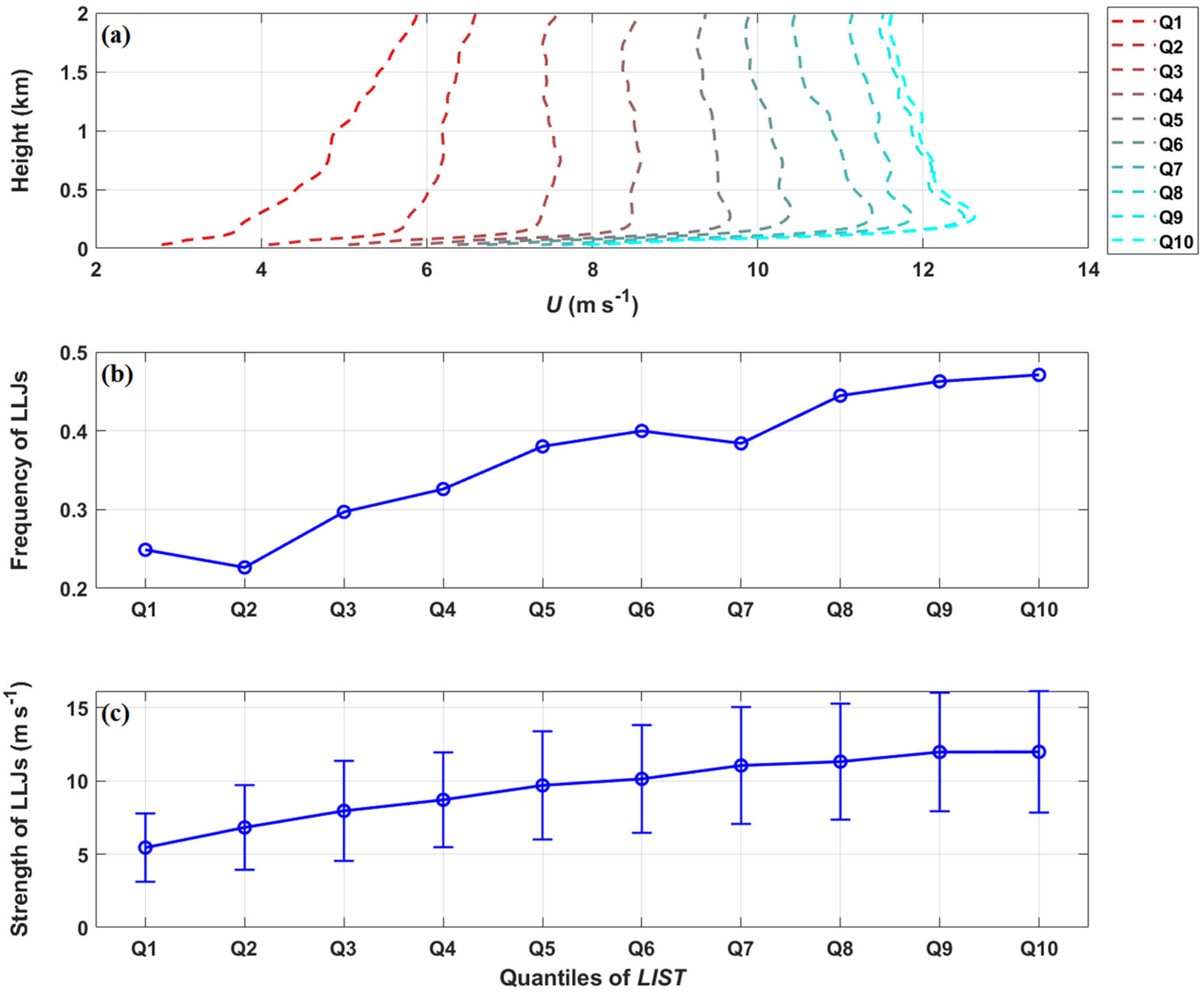

Figure 8. (a) The vertical structures of wind speed within the atmospheric boundary layer, (b) the frequency of LLJs, and (c) the strength of LLJs under different intermittency conditions.

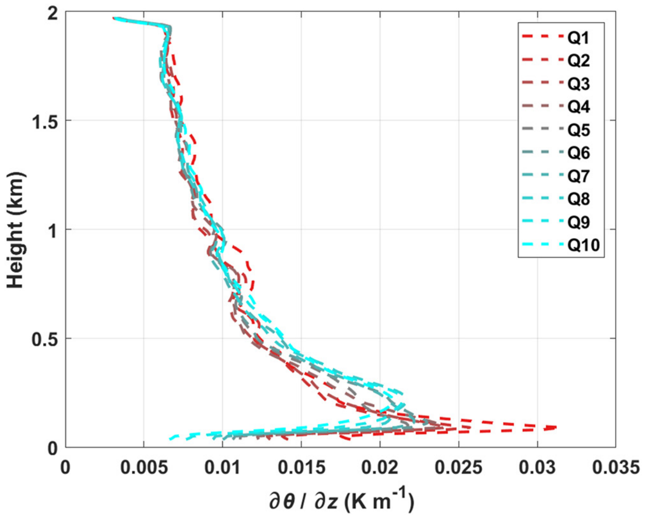

Figure 9. The vertical potential temperature gradient within the atmospheric boundary layer under different intermittency strength conditions.

nocturnal boundary layer. Another notable distinction of wind speed profiles under different intermittency strength situations is related to LLJs. To quantify the characteristics of LLJs, a criterion proposed based on the MOSAiC radiosondes for LLJ detection is adopted (López-García et al., 2022). Our results show that LIST is related to the occurrence frequency of LLJs. As the occurrence frequency of LLJs decreases, LIST increases gradually. On the other hand, strong LLJs generally occur when turbulent motions are strong, while weak LLJs correspond to periods of strong intermittency. The mean strength of the LLJs in Q1 is only 5.5 m s^{-1}, but this value reaches up to 12.0 m s^{-1} in Q10. Banta et al. (2003) and Mahrt (2014) both concluded that the contribution of LLJs is to produce enhanced vertical shear that further leads to turbulence production in the surface layer of a stable boundary layer.

3.3.2. The Role of Temperature Inversions

Figure 9 compares the vertical potential temperature gradient ($\partial\theta/\partial z$) within the atmospheric boundary layer under different intermittency strength conditions. Strong temperature inversions prevail in the boundary layer over the Arctic sea-ice surface, especially in winter, indicating that buoyancy's contribution to turbulent motions within the surface layer is negative. Although there is no conspicuous rule for the variation of vertical potential temperature gradient with intermittency strength in the upper level of the boundary layer (above 0.5 km), the vertical structure of potential temperature below 0.5 km reveals that strong, low-level temperature inversions lead to an increase in intermittency strength. Under the strongest intermittency condition (i.e., Q1), the maximum vertical potential temperature gradient reaches 0.032 K m^{-1} at the height of 0.09 km; however, the maximum vertical potential temperature gradient is just 0.021 K m^{-1} at the height of 0.21 km when LIST is in the Q10 interval. The signal of suppressed turbulence under strong inversion situations was also found during the CASES-99 (Cooperative Atmosphere-Surface Exchange Study in 1999) experiment (Sun et al., 2012).

4. Summary

Using the data collected during the MOSAiC expedition, we propose a new algorithm to identify the spectral gap between submesoscale and turbulent motions in this study. Based on analysis of the reconstructed signal of turbulent and submesoscale motions, the characteristics of turbulent intermittency within the atmospheric surface layer over the Arctic sea-ice surface are investigated.

Submesoscale motions significantly affect surface fluxes calculated using the EC method throughout the MOSAiC expedition. The relationship between LIST and near-surface conventional meteorological conditions reveals that LIST increases with the increase of wind speed and wind speed gradient and with the decrease of the air temperature gradient. In addition, our results show that turbulence intermittency under stable stratification is stronger than that under unstable stratification, and the turbulence signal under near-neutral stratification is the purest. Surface fluxes calculated using the EC method and raw turbulent fluctuations are overestimated. The overestimation of momentum flux, sensible heat flux, and latent heat flux is 3%, 10%, and 24%, respectively. Hence, nonstationary motions have the greatest relative influence on the latent heat flux over the Arctic sea-ice surface, although the latent heat flux in this region is typically small. By investigating the characteristics of atmospheric boundary layer structure under different intermittency strength conditions, we found that strong LLJs are conducive to turbulence production in the surface layer of the stable boundary layer, while weak LLJs correspond to strong turbulence intermittency. Additionally, strong, low-level temperature inversions suppress turbulent motions and lead to strong intermittency.

This study reveals the characteristics of turbulent intermittency over the Arctic sea-ice surface during the year-long MOSAiC expedition. In addition, we provide an automatic algorithm for correcting the impact of nonstationary motions when calculating surface fluxes via the EC method in the polar regions, although the empirical parameters in this algorithm might be site-dependent. Broadly for different sites, the identified empirical parameters in the newly proposed automatic algorithm could be tested as to when the resultant turbulent kinetic energy in both turbulent signal and submesoscale signal obey a nonlinear Langevin model as suggested by Allouche et al. (2021). However, although the effects of submesoscale motions on surface turbulent fluxes have been quantified in this study, the mechanism of generation and development of submesoscale motions remains to be clarified. To achieve this, we must incorporate large-eddy simulation experiments, and this work will be carried out in the future.

Acknowledgments
Data used in this manuscript were produced as part of the international Multidisciplinary drifting Observatory for the Study of Arctic Climate (MOSAiC) expedition with tag MOSAiC20192020. We thank all persons involved in the expedition of the Research Vessel Polarstern during MOSAiC in 2019–2020 (AWI_PS122_00) as listed in Nixdorf et al. (2021). A subset of data was obtained from the Atmospheric Radiation Measurement (ARM) User Facility, a US Department of Energy (DOE) Office of Science User Facility Managed by the Biological and Environmental Research Program. The University of Colorado/NOAA surface flux team are acknowledged for their efforts in collecting and post-processing the near-surface flux and meteorological measurements. The Alfred Wegener Institute and German Weather Service are acknowledged for their contributions to the MOSAiC sounding program, with support from the DOE ARM program. This study is supported by the National Natural Science Foundation of China (Nos. 42105072, 41922044, 41941009), the National Key Research and Development Program of China (No. 2022YFE0106300), the Guangdong Basic and Applied Basic Research Foundation (Nos. 2021A1515012209, 2020B1515020025), the China Postdoctoral Science Foundation (Nos. 2021M693585), and the Norges Forskningsråd (Grant 328886). MDS was supported by the US National Science Foundation (OPP-1724551), the DOE Atmospheric System Research Program (DE-SC0021341, DE_SC0023036), and the National Oceanic and Atmospheric Administration Physical Sciences Laboratory under cooperative agreement (NA22OAR4320151).

Data Availability Statement

The interpolated sounding (Jensen et al., 2019) and precipitation (Wang et al., 2019) data are available from the US Department of Energy Atmospheric Radiation Measurement Program archive at http://dx.doi.org/10.5439/1095316 and http://dx.doi.org/10.5439/1779709, respectively. The MOSAiC surface flux and other meteorological data are available at the Arctic Data Center at http://dx.doi.org/10.18739/A2VM42Z5F (Cox et al., 2021) and http://dx.doi.org/10.18739/A2PV6B83F (Cox et al., 2023).

References

Acevedo, O. C., Costa, F. D., Oliveira, P. E. S., Puhales, F. S., Degrazia, G. A., & Roberti, D. R. (2014). The influence of submeso processes on stable boundary layer similarity relationships. *Journal of the Atmospheric Sciences*, *71*(1), 207–225. https://doi.org/10.1175/JAS-D-13-0131.1

Acevedo, O. C., Moraes, O. L. L., Degrazia, G. A., & Medeiros, L. E. (2006). Intermittency and the exchange of scalars in the nocturnal surface layer. *Boundary-Layer Meteorology*, *119*(1), 41–55. https://doi.org/10.1007/s10546-005-9019-3

Allouche, M., Bou-Zeid, E., Ansorge, C., Katul, G. G., Chamecki, M., Acevedo, O., et al. (2022). The detection, genesis, and modeling of turbulence intermittency in the stable atmospheric surface layer. *Journal of the Atmospheric Sciences*, *79*(4), 1171–1190. https://doi.org/10.1175/JAS-D-21-0053.1

Allouche, M., Katul, G. G., Fuentes, J. D., & Bou-Zeid, E. (2021). Probability law of turbulent kinetic energy in the atmospheric surface layer. *Physical Review Fluids*, *6*(7). https://doi.org/10.1103/physrevfluids.6.074601

Andreas, E. L., Horst, T. W., Grachev, A. A., Persson, P. O. G., Fairall, C. W., Guest, P. S., & Jordan, R. E. (2010). Parametrizing turbulent exchange over summer sea ice and the marginal ice zone. *Quarterly Journal of the Royal Meteorological Society*, *136*(649), 927–943. https://doi.org/10.1002/qj.618

Anfossi, D., Oettl, D., Degrazia, G., & Goulart, A. (2005). An analysis of sonic anemometer observations in low wind speed conditions. *Boundary-Layer Meteorology*, *114*(1), 179–203. https://doi.org/10.1007/s10546-004-1984-4

Ansorge, C., & Mellado, J. P. (2014). Global intermittency and collapsing turbulence in the stratified planetary boundary layer. *Boundary-Layer Meteorology*, *153*(1), 89–116. https://doi.org/10.1007/s10546-014-9941-3

Ansorge, C., & Mellado, J. P. (2016). Analyses of external and global intermittency in the logarithmic layer of Ekman flow. *Journal of Fluid Mechanics*, *805*, 611–635. https://doi.org/10.1017/jfm.2016.534

Aubinet, M., Feigenwinter, C., Heinesch, B., Laffineur, Q., Papale, D., Reichstein, M., et al. (2012). Nighttime flux correction. In M. Aubinet, T. Vesala, & D. Papale (Eds.), *Eddy covariance: A practical guide to measurement and data analysis* (pp. 133–157). Springer Netherlands. https://doi.org/10.1007/978-94-007-2351-1_5

Banta, R. M., Pichugina, Y. L., & Newsom, R. K. (2003). Relationship between low-level jet properties and turbulence kinetic energy in the nocturnal stable boundary layer. *Journal of the Atmospheric Sciences*, *60*(20), 2549–2555. https://doi.org/10.1175/1520-0469(2003)060<2549:rbljpa>2.0.CO;2

Best, M. J., Pryor, M., Clark, D. B., Rooney, G. G., Essery, R. L. H., Ménard, C. B., et al. (2011). The joint UK **land environment simu**lator (JULES), model description – Part 1: Energy and water fluxes. *Geoscientific Model Development*, *4*(3), 677–699. https://doi.org/10.5194/gmd-4-677-2011

Cava, D., Mortarini, L., Anfossi, D., & Giostra, U. (2019). Interaction of submeso motions in the Antarctic stable boundary layer. *Boundary-Layer Meteorology*, *171*(2), 151–173. https://doi.org/10.1007/s10546-019-00426-7

Cava, D., Mortarini, L., Giostra, U., Richiardone, R., & Anfossi, D. (2017). A wavelet analysis of low wind speed submeso motions in a nocturnal boundary layer. *Quarterly Journal of the Royal Meteorological Society*, *143*(703), 661–669. https://doi.org/10.1002/qj.2954

Coulter, R. L., & Doran, J. C. (2002). Spatial and temporal occurrences of intermittent turbulence during CASES-99. *Boundary-Layer Meteorology*, *105*(2), 329–349. https://doi.org/10.1023/A:1019993703820

Cox, C., Gallagher, M., Shupe, M., Persson, O., Blomquist, B., Grachev, A., et al. (2023). Met city meteorological and surface flux measurements (level 3 final), multidisciplinary drifting observatory for the study of Arctic climate (MOSAiC), central Arctic, October 2019 - September 2020 [Dataset]. Arctic Data Center. https://doi.org/10.18739/A2PV6B83F

Cox, C., Gallagher, M., Shupe, M., Persson, O., Solomon, A., Blomquist, B., et al. (2021). 10-meter (m) meteorological flux tower measurements (level 1 raw), multidisciplinary drifting observatory for the study of Arctic climate (MOSAiC), central Arctic, October 2019–September 2020 [Dataset]. Arctic Data Center. https://doi.org/10.18739/A2VM42Z5F

Doran, J. C. (2004). Characteristics of intermittent turbulent temperature fluxes in stable conditions. *Boundary-Layer Meteorology*, *112*(2), 241–255. https://doi.org/10.1023/b:boun.0000027907.06649.d0

Drüe, C., & Heinemann, G. (2007). Characteristics of intermittent turbulence in the upper stable boundary layer over Greenland. *Boundary-Layer Meteorology*, *124*(3), 361–381. https://doi.org/10.1007/s10546-007-9175-8

Fiedler, F., & Panofsky, H. A. (1970). Atmospheric scales and spectral gaps. *Bulletin of the American Meteorological Society*, *51*(12), 1114–1120. https://doi.org/10.1175/1520-0477(1970)051<1114:ASASG>2.0.CO;2

Grachev, A. A., Fairall, C. W., Persson, P. O. G., Andreas, E. L., & Guest, P. S. (2005). Stable boundary-layer scaling regimes: The SHEBA data. *Boundary-Layer Meteorology*, *116*(2), 201–235. https://doi.org/10.1007/s10546-004-2729-0

Helmis, C. G., Sgouros, G., & Wang, Q. (2015). On the vertical structure and spectral characteristics of the marine Low-Level Jet. *Atmospheric Research*, *152*, 74–81. https://doi.org/10.1016/j.atmosres.2013.11.005

Howell, J. F., & Mahrt, L. (1997). Multiresolution flux decomposition. *Boundary-Layer Meteorology*, *83*(1), 117–137. https://doi.org/10.1023/A:1000210427798

Huang, Y. X., Schmitt, F. G., Hermand, J. P., Gagne, Y., Lu, Z. M., & Liu, Y. L. (2011). Arbitrary-order Hilbert spectral analysis for time series possessing scaling statistics: Comparison study with detrended fluctuation analysis and wavelet leaders. *Physical Review E*, *84*(1), 16208. https://doi.org/10.1103/PhysRevE.84.016208

Huang, Y. X., Schmitt, F. G., Lu, Z. M., & Liu, Y. L. (2008). An amplitude-frequency study of turbulent scaling intermittency using Empirical Mode Decomposition and Hilbert Spectral Analysis. *Europhysics Letters*, *84*(4), 40010. https://doi.org/10.1209/0295-5075/84/40010

Jensen, M., Giangrande, S., Fairless, T., & Zhou, A. (2019). Interpolated sonde (INTERPOLATEDSONDE), Atmospheric radiation measurement (ARM) user facility [Dataset]. ARM Data Center. https://doi.org/10.5439/1095316

Knust, R. (2017). Polar research and supply vessel POLARSTERN operated by the Alfred-Wegener-Institute. *Journal of Large-Scale Research Facilities*, *3*, A119. https://doi.org/10.17815/jlsrf-3-163

Kwok, R., & Cunningham, G. F. (2015). Variability of Arctic sea ice thickness and volume from CryoSat-2. *Philosophical Transactions of the Royal Society A*, *373*(2045), 20140157. https://doi.org/10.1098/rsta.2014.0157

Landrum, L., & Holland, M. M. (2020). Extremes become routine in an emerging new Arctic. *Nature Climate Change*, *10*(12), 1–8. https://doi.org/10.1038/s41558-020-0892-z

Li, X., Gao, C. Y., Gao, Z., & Zhang, X. (2020). Atmospheric boundary layer turbulence structure for severe foggy haze episodes in north China in December 2016. *Environmental Pollution*, *264*, 114726. https://doi.org/10.1016/j.envpol.2020.114726

Lu, Y., Zhou, M., & Wu, T. (2013). Validation of parameterizations for the surface turbulent fluxes over sea ice with CHINARE 2010 and SHEBA data. *Polar Research*, *32*(1), 20818. https://doi.org/10.3402/polar.v32i0.20818

López-García, V., Neely, R. R., III, Dahlke, S., & Brooks, I. M. (2022). Low-level jets over the Arctic ocean during MOSAiC. *Elementa Science of the Anthropocene*, *10*, 1. https://doi.org/10.1525/elementa.2022.00063

Mahrt, L. (1999). Stratified atmospheric boundary layers. *Boundary-Layer Meteorology*, *90*(3), 375–396. https://doi.org/10.1023/A:1001765727956

Mahrt, L. (2007). Weak-wind mesoscale meandering in the nocturnal boundary layer. *Environmental Fluid Mechanics*, *7*(4), 331–347. https://doi.org/10.1007/s10652-007-9024-9

Mahrt, L. (2009). Characteristics of submeso winds in the stable boundary layer. *Boundary-Layer Meteorology*, *130*, 1–14. https://doi.org/10.1007/s10546-008-9336-4

Mahrt, L. (2010). Variability and maintenance of turbulence in the very stable boundary layer. *Boundary-Layer Meteorology*, *135*, 1–18. https://doi.org/10.1007/s10546-009-9463-6

Mahrt, L. (2014). Stably stratified atmospheric boundary layers. *Annual Review of Fluid Mechanics*, *46*(1), 23–45. https://doi.org/10.1146/annurevfluid-010313-141354

Mahrt, L. (2019). Microfronts in the nocturnal boundary layer. *Quarterly Journal of the Royal Meteorological Society*, *145*(719), 546–562. https://doi.org/10.1002/qj.3451

Mahrt, L., & Bou-Zeid, E. (2020). Non-stationary boundary layers. *Boundary-Layer Meteorology*, *177*(2–3), 189–204. https://doi.org/10.1007/s10546-020-00533-w

Monahan, A. H., Rees, T., He, Y., & McFarlane, N. (2015). Multiple regimes of wind, stratification, and turbulence in the stable boundary layer. *Journal of the Atmospheric Sciences*, *72*(8), 3178–3198. https://doi.org/10.1175/JAS-D-14-0311.1

Mortarini, L., Cava, D., Giostra, U., Costa, F. D., Degrazia, G., Anfossi, D., & Acevedo, O. (2019). Horizontal meandering as a distinctive feature of the stable boundary layer. *Journal of the Atmospheric Sciences*, *76*(10), 3029–3046. https://doi.org/10.1175/JAS-D-18-0280.1

Muschinski, A., Frehlich, R. G., & Balsley, B. B. (2004). Small-scale and large-scale intermittency in the nocturnal boundary layer and the residual layer. *Journal of Fluid Mechanics*, *515*, 319–351. https://doi.org/10.1017/S0022112004000412

Nixdorf, U., Dethloff, K., Rex, M., Shupe, M., Sommerfeld, A., Perovich, D. K., et al. (2021). MOSAiC extended acknowledgement. *Zenodo*. https://doi.org/10.5281/zenodo.5541624

Peltola, O., Aslan, T., Ibrom, A., Nemitz, E., Rannik, U., & Mammarella, I. (2021). The high-frequency response correction of eddy covariance fluxes – Part 1: An experimental approach and its interdependence with the time-lag estimation. *Atmospheric Measurement Techniques*, *14*(7), 5071–5088. https://doi.org/10.5194/amt-14-5071-2021

Ren, Y., Zhang, H. S., Wei, W., Wu, B. G., Cai, X. H., & Song, Y. (2019). Effects of turbulence structure and urbanization on the heavy haze pollution process. *Atmospheric Chemistry and Physics*, *19*(2), 1041–1057. https://doi.org/10.5194/acp-19-1041-2019

Ren, Y., Zhang, H. S., Wei, W., Wu, B. G., Liu, J. L., Cai, X. H., & Song, Y. (2019). Comparison of the turbulence structure during light and heavy haze pollution episodes. *Atmospheric Research*, *230*, 104645. https://doi.org/10.1016/j.atmosres.2019.104645

Rilling, G., Patrick, F., & Paulo, G. (2003). On empirical mode decomposition and its algorithms. In *IEEE-EURASIP workshop on nonlinear signal and image processing* (pp. 8–11). NSIP-03.

Salmond, J. A., & McKendry, I. G. (2005). A review of turbulence in the very stable nocturnal boundary layer and its implications for air quality. *Progress in Physical Geography: Earth and Environment*, *29*(2), 171–188. https://doi.org/10.1191/0309133305pp442ra

Schmitt, F. G., Huang, Y., Lu, Z., Liu, Y., & Fernandez, N. (2009). Analysis of velocity fluctuations and their intermittency properties in the surf zone using empirical mode decomposition. *Journal of Marine Systems*, *77*(4), 473–481. https://doi.org/10.1016/j.jmarsys.2008.11.012

Shupe, M. D., Rex, M., Blomquist, B., Persson, P. O. G., Schmale, J., Uttal, T., et al. (2022). Overview of the MOSAiC expedition: Atmosphere. *Elementa Science of the Anthropocene*, *10*(1). https://doi.org/10.1525/elementa.2021.00060

Sorbjan, Z., & Czerwinska, A. (2013). Statistics of turbulence in the stable boundary layer affected by gravity waves. *Boundary-Layer Meteorology*, *148*(1), 73–91. https://doi.org/10.1007/s10546013-9809-y

Sun, J., Mahrt, L., Banta, R. M., & Pichugina, Y. L. (2012). Turbulence regimes and turbulence intermittency in the stable boundary layer during CASES-99. *Journal of the Atmospheric Sciences*, *69*(1), 338–351. https://doi.org/10.1175/jas-d-11-082.1

Sun, J., Mahrt, L., Nappo, C., & Lenschow, D. H. (2015). Wind and temperature oscillations generated by wave–turbulence interactions in the stably stratified boundary layer. *Journal of the Atmospheric Sciences*, *72*(4), 1484–1503. https://doi.org/10.1175/JAS-D-14-0129.1

Terradellas, E., Soler, M. R., Ferreres, E., & Bravo, M. (2005). Analysis of oscillations in the stable atmospheric boundary layer using wavelet methods. *Boundary-Layer Meteorology*, *114*(3), 489–518. https://doi.org/10.1007/s10546-004-1293-y

van den Kroonenberg, A., & Bange, J. (2007). Turbulent flux calculation in the polar stable boundary layer: Multiresolution flux decomposition and wavelet analysis. *Journal of Geophysical Research*, *112*(D6), D06112. https://doi.org/10.1029/2006JD007819

Van de Wiel, B. J. H., Moene, A. F., Jonker, H. J. J., Baas, P., Basu, S., Donda, J. M. M., et al. (2012). The minimum wind speed for sustainable turbulence in the nocturnal boundary layer. *Journal of the Atmospheric Sciences*, *69*(11), 3116–3127. https://doi.org/10.1175/JAS-D-12-0107.1

Vickers, D., & Mahrt, L. (2003). The cospectral gap and turbulent flux calculations. *Journal of Atmospheric and Oceanic Technology*, *20*(5), 660–672. https://doi.org/10.1175/1520-0426(2003)20<660:TCGATF>2.0.CO;2

Vickers, D., & Mahrt, L. (2006). A solution for flux contamination by mesoscale motions with very weak turbulence. *Boundary-Layer Meteorology*, *118*(3), 431–447. https://doi.org/10.1007/s10546005-9003-y

Wang, D., Bartholomew, M. J., & Shi, Y. (2019). Laser disdrometer (LD), atmospheric radiation measurement (ARM) user facility [Dataset]. ARM. https://doi.org/10.5439/1779709

Wei, W., Zhang, H., Wu, B., Huang, Y., Cai, X., Song, Y., & Li, J. (2018). Intermittent turbulence contributes to vertical dispersion of PM2:5 in the north China plain: Cases from Tianjin. *Atmospheric Chemistry and Physics*, *18*(17), 12953–12967. https://doi.org/10.5194/acp-18-12953-2018

Wei, W., & Zhang, H. S. (2013). The Hilbert-Huang transform technique and its applications to the study of the turbulence boundary layer. *Acta Meteorologica Sinica*, *6*, 1183–1193. https://doi.org/10.11676/qxxb2013.096

Wei, W., Zhang, H. S., Cai, X. H., Song, Y., Bian, Y. X., Xiao, K. T., & Zhang, H. (2020). Influence of intermittent turbulence on air pollution and its dispersion in winter 2016/2017 over Beijing, China. *Journal of Meteorological Research*, *34*(1), 176–188. https://doi.org/10.1007/s13351-020-9128-4

Wei, W., Zhang, H. S., Schmitt, F. G., Huang, Y. X., Cai, X. H., Song, Y., et al. (2017). Investigation of turbulence behaviour in the stable boundary layer using arbitrary order Hilbert spectra. *Boundary-Layer Meteorology*, *163*(2), 311–326. https://doi.org/10.1007/s10546-016-0227-9

Wei, Z. R., Zhang, L., Ren, Y., Wei, W., Zhang, H. S., Cai, X. H., et al. (2021). Characteristics of the turbulence intermittency and its influence on the turbulent transport in the semi-arid region of the Loess Plateau. *Atmospheric Research*, *249*, 105312. https://doi.org/10.1016/j.atmosres.2020.105312

Zilitinkevich, S., & Calanca, P. (2000). An extended similarity theory for the stably stratified atmospheric surface layer. *Quarterly Journal of the Royal Meteorological Society*, *126*(566), 1913–1923. https://doi.org/10.1002/qj.49712656617